ADVANCED FUNCTIONAL MATERIALS
www.afm-journal.de

Defect Analysis of the β– to γ–Ga_2O_3 Phase Transition

Umutcan Bektas, Maciej O. Liedke, Huan Liu, Fabian Ganss, Maik Butterling, Nico Klingner, René Hübner, Ilja Makkonen, Andreas Wagner, and Gregor Hlawacek**

This study investigates the ion irradiation induced phase transition in gallium oxide (Ga_2O_3) from the β to the γ phase, the role of defects during the transformation, and the quality of the resulting crystal structure. Using a multi-method analysis approach including X-ray diffraction (XRD), transmission electron microscopy (TEM), Rutherford backscattering spectrometry in channeling mode (RBS/c), Doppler broadening variable energy positron annihilation spectroscopy (DB-VEPAS), and variable energy positron annihilation lifetime spectroscopy (VEPALS) supported by density functional theory (DFT) calculations, defects at all the relevant stages of the phase transition are characterized. A reduction in backscattering yield is observed in RBS/c spectra after the transition to the γ phase. This goes hand in hand with a significant decrease in the positron trapping center density due to generation of embedded vacancies intrinsic for the γ–Ga_2O_3 but too shallow in order to trap positrons. A comparison of the observed positron lifetime of γ–Ga_2O_3 with different theoretical models shows good agreement with the three-site γ phase approach. A characteristic increase in the effective positron diffusion length and the positron lifetime at the transition point from β–Ga_2O_3 to γ–Ga_2O_3 enables visualization of the phase transition with positrons for the first time. Moreover, a subsequent reduction of these quantities with increasing irradiation fluence is observed, which attributes to further evolution of the γ–Ga_2O_3 and changes in the gallium vacancy density as well as relative occupation in the crystal lattice.

1. Introduction

Throughout the history of science and engineering, there has always been a drive to find new and superior materials to advance technology. This is also true for power electronics, which needs new materials and related research activities to ensure future developments. Gallium oxide (Ga_2O_3) is a promising candidate for future ultrawide-bandgap (UWB) semiconductor materials for power electronic devices. It has two main advantages over the traditional UWB semiconductor materials, such as silicon carbide and gallium nitride. Ga_2O_3 does not only have a superior breakdown voltage, which allows to increase the device performance,[1] but cost-effective large wafer production by melt growth methods is also possible with Ga_2O_3.[2] Furthermore, the existence of different polymorphs of Ga_2O_3 makes it a compelling material for crystal structure engineering. This might be achieved via fabrication of different polymorphic layers on a single wafer as well as engineering of nanostructures with different polymorphs. However, most research has focused on the β phase, which is the most chemically and thermally stable polymorph of Ga_2O_3.[3]

Ion implantation is a well-established method for enhancing the properties of semiconductors, and several attempts have been made to dope β–Ga_2O_3.[4–6] Low-fluence rare-earth heavy ion irradiation has been employed to enhance the luminescence properties of β–Ga_2O_3; however, ion-induced damage and the resulting structural disorder have negatively impacted luminescence performance.[7–9] Recently, Azarov et al. demonstrated the high radiation tolerance of double-polymorph γ/β Ga_2O_3 structures.[10] Furthermore, Azarov et al. demonstrated that the fabrication of multilayer γ/β polymorph structures is possible through controlled dynamic annealing.[11] This property makes Ga_2O_3 a good candidate for future electronic devices in space and nuclear applications, where radiation tolerance is key to ensuring consistent performance of electrical devices over decades.[12] Attempts were made to increase the n-type conductivity of Ga_2O_3, and success was reported for silicon,[6] tin,[13] and hydrogen doping.[14,15] However, the desired high n-type conductivity has not yet been achieved due to existing compensation centers in Ga_2O_3, i.e., gallium mono-vacancies.[16,17]

U. Bektas, F. Ganss, N. Klingner, R. Hübner, G. Hlawacek
Institute of Ion Beam Physics and Materials Research
Helmholtz-Zentrum Dresden – Rossendorf e.V.
Bautzner Landstrasse 400, 01328 Dresden, Germany
E-mail: u.bektas@hzdr.de; g.hlawacek@hzdr.de

M. O. Liedke, A. Wagner
Institute of Radiation Physics
Helmholtz-Zentrum Dresden – Rossendorf e.V.
Bautzner Landstrasse 400, 01328 Dresden, Germany

H. Liu, I. Makkonen
Department of Physics
University of Helsinki
P.O.Box 43, University of Helsinki FI-00014, Finland

M. Butterling
Reactor Institute Delft
Delft University of Technology
Mekelweg 15, NI-2629 JB Delft, The Netherlands

The ORCID identification number(s) for the author(s) of this article can be found under https://doi.org/10.1002/adfm.202509688

DOI: 10.1002/adfm.202509688

Therefore, it is crucial to study and understand the formation of gallium-vacancy-related defects of the various Ga_2O_3 polymorphs in their pristine state as well as during the phase transitions. The latter is relevant to the design of future radiation-tolerant electronic devices in which the polymorphs of Ga_2O_3 would be exploited to create new functionality. It has been observed that high-energy and high-fluence ion irradiation, beyond a certain threshold, can induce a phase transition from the β phase to the γ phase of Ga_2O_3 instead of amorphization.[10] According to recent studies, the β-to-γ phase transition may restrain the amorphization mechanism.[18] This transition competes with amorphization and is driven by increased structural disorder and accumulated strain, which promote favorable atomic rearrangements.[10,19,20] A key driving factor for the transition from the monoclinic β phase to the defective spinel γ phase is the preservation of a stable and similar oxygen sublattice.[10,18,21] Huang et al. demonstrated the atomic-scale mechanism of this transition and concluded that the relaxation of point defects at high concentrations, driven by lattice strain, plays a critical role.[20] Fernández et al. also showed that the transition occurs independently of the implanted ion species.[22]

Here, we present a multi-method analysis approach (X-ray diffraction (XRD), transmission electron microscopy (TEM), RBS/c, Doppler broadening variable energy positron annihilation spectroscopy (DB-VEPAS), and variable energy positron annihilation lifetime spectroscopy (VEPALS), both supported by density functional theory (DFT) calculations) to better understand the role of atomic defects for the β–Ga_2O_3 to γ–Ga_2O_3 phase transition. Defect formation and polymorph conversion are triggered by ion beam irradiation with noble gas ions to exclude chemical influences on the observed effects. Our results offer unique insights into the defects in ion-beam-induced γ–Ga_2O_3 and contribute to a deeper understanding of its radiation tolerance mechanisms.

2. Results and Discussion

In this study, commercial ($\bar{2}$ 0 1)-oriented β–Ga_2O_3 substrates were irradiated with different fluences of 140 keV Ne^+. XRD and TEM were performed to confirm the phase transition, as shown in **Figure 1**. Based on the presented $\theta/2\theta$ scans in Figure 1a,b and Note S1 (Supporting Information), we conclude that the γ phase formed with (1 1 1) orientation. The 111, 222, 333, and 444 γ–Ga_2O_3 reflections should usually be observable within a 2θ range from 10° to 90°. However, only the γ 222 and γ 444 reflections are visible in our $\theta/2\theta$ scans. As discussed in Note S1 (Supporting Information), this apparent inconsistency is attributed to the presence of antiphase boundarys (APBs) in the γ phase,[23–25] which induce destructive interference, thereby suppressing the γ 111 and γ 333 reflections. To focus on the γ 444 reflection, only a small section of the XRD patterns is presented here; the full diffractogram can be found in Note S1 (Supporting Information).

For all samples, the $\bar{8}04$ reflection of β–Ga_2O_3 at about 82.2° is expected due to diffraction from the unaffected substrate underneath the irradiated layer, whose thickness is less than the X-ray penetration depth. If a γ layer is present on top of the β–Ga_2O_3, an additional peak near 80.2° is visible, which is identified as the 444 reflection of γ–Ga_2O_3. As shown in Figure 1a, after irradiation with a fluence of 3.5×10^{14} ion cm^{-2}, an asymmetric shoulder of the $\bar{8}04$ reflection appears due to the lattice distortion and defect formation in the β–Ga_2O_3 crystal. Increasing the fluence by one order of magnitude to 3.5×10^{15} ion cm^{-2} results in a distinct peak at 80.5°, which is close to the characteristic 444 reflection of γ–Ga_2O_3. The irradiation fluence corresponds to a peak damage of 2.6 displacements per atom (dpa) (see Note S2, Supporting Information), which is still one order of magnitude less than the dpa required to induce the phase transition.[10] Therefore, we conclude that at a fluence of 3.5×10^{15} ion cm^{-2}, the transition from the β to the γ phase has already started locally in small, highly damaged pockets but is not yet complete.

In Figure 1b, after a further increase of the fluence by a factor of ten (3.5×10^{16} ion cm^{-2}), corresponding to a peak damage of 26 dpa, the 444 reflection of the γ phase appears clearly at the expected position. The broadening of the γ 444 peak suggests the presence of inhomogeneous strain and lattice defects within the γ layer.

It is important to note that the β-to-γ phase transition occurs independently of the substrate's surface orientation[22] and is, to a large extent, also independent of the used ion species and energy.[10] The former statement is confirmed by the observed conversion to the γ phase for (0 1 0)-oriented substrates following 140 keV Ne^+ irradiation with a fluence of 3.5×10^{16} ion cm^{-2} (see Note S1, Supporting Information).

Increasing the fluence further to 7.0×10^{16} ion cm^{-2} (52 dpa) broadens the $\bar{8}04$ reflection asymmetrically towards a larger lattice plane spacing most likely due to strain accumulation. After applying 3.5×10^{17} ion cm^{-2}, which corresponds to 260 dpa, the γ 444 reflection vanishes almost completely, likely due to significant disorder within the γ layer.

In the BF-STEM image shown in Figure 1c, the converted layer is visible with a thickness of ≈ 260 nm after 140 keV Ne^+ irradiation with a fluence of 3.5×10^{16} ion cm^{-2}. The FFT patterns shown in Figure 1d,e correspond to the regions marked in blue and red in Figure 1c, respectively. The FFTs obtained from the different regions confirm that the top layer has the defective spinel cubic structure of γ–Ga_2O_3, while the unaffected substrate has the original monoclinic crystal structure of β–Ga_2O_3. As is evident from Figure 1c, the γ layer shows severe damage in particular close to the β/γ interface. As can easily be observed in Figure 1d, several diffraction spots in the FFT pattern of the cubic γ phase, such as the {1 1 1} reflections (highlighted in blue circles), are blurry and suspected of spot broadening compared to the sharper FFT pattern of the monoclinic β phase in Figure 1e. We attribute the spot broadening to crystal imperfections arising from the ion beam irradiation and the intrinsic vacancies present even in a perfect defective spinel structure as is the case here.

Different from the XRD results presented above, we do observe weak and broad {1 1 1} reflections in the FFT pattern of the Ne^+-irradiated layer. Careful analysis of the TEM samples using selected-area electron diffraction and convergent-beam electron diffraction confirms that due to the small number of APBs present in the limited volume of the TEM sample, the extinction of the {1 1 1} peaks is not perfect and they appear as broad and weak spots in the FFT.

In **Figure 2**, RBS/c spectra are plotted for Ga_2O_3 after Ne^+ implantation of different fluencies to check the crystal quality

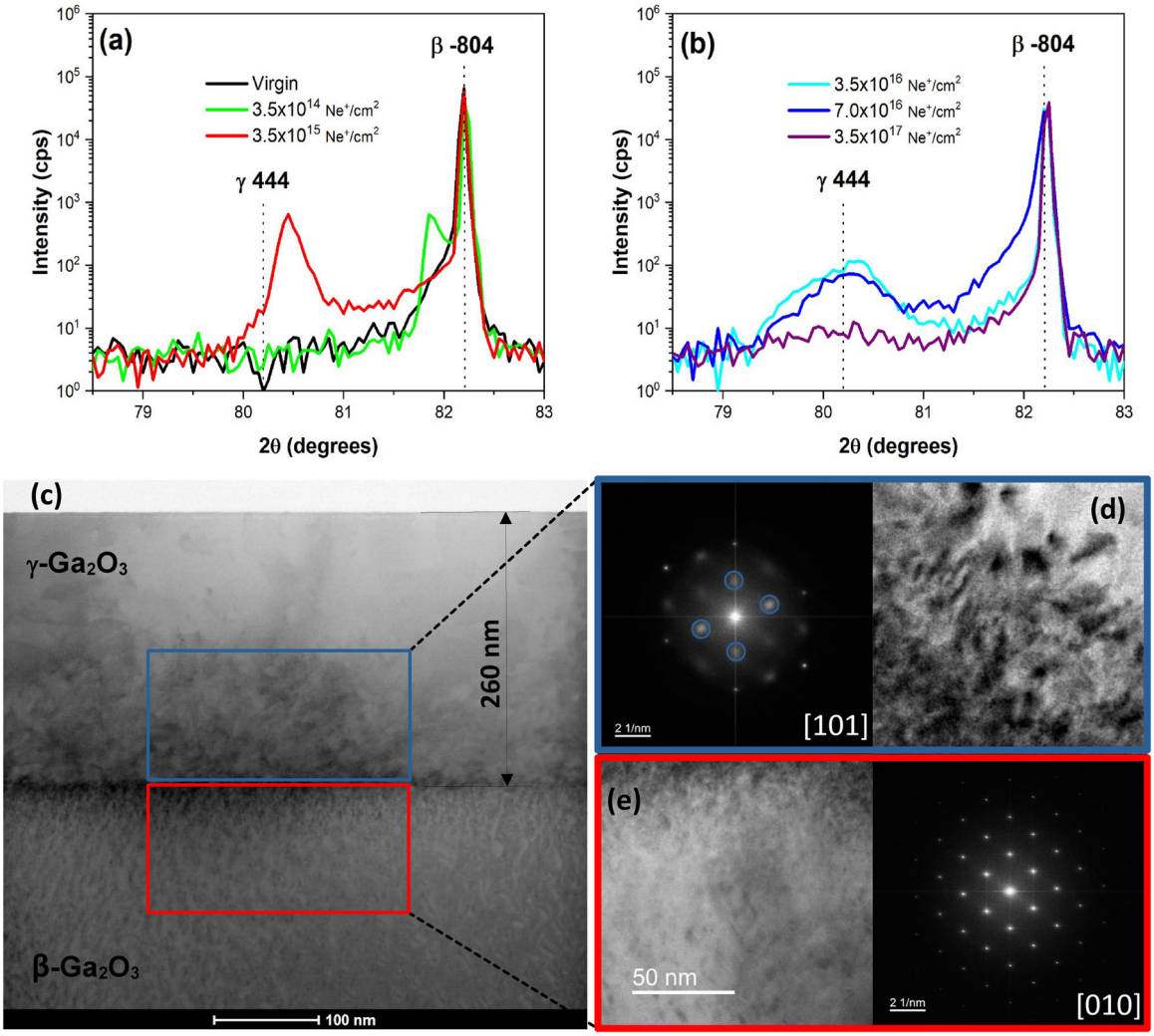

Figure 1. Structure analysis of β–Ga_2O_3 irradiated with different fluences of 140 keV Ne^+. a) XRD patterns of the virgin and irradiated samples with low fluences, b) XRD patterns of the irradiated samples with high fluences. c) bright-field scanning transmission electron microscopy (BF-STEM) image of the converted layer on top of pristine β–Ga_2O_3. d) high-resolution transmission electron microscopy (HRTEM) image (right) and fast Fourier transform (FFT) (left) of the γ layer close to the interface along [1 0 1] zone axis. The diffraction spots highlighted by the blue circles correspond to the γ–Ga_2O_3 {1 1 1} reflections. e) HRTEM image and FFT pattern of the β region close to the interface along [0 1 0] zone axis.

after the irradiation. Two sets of spectra are presented. While the RBS/c spectra for β-Ga_2O_3 and γ-Ga_2O_3 presented in Figure 2a were obtained with the ion beam parallel to the β-Ga_2O_3–[$\bar{2}$ 0 1] direction, the ion beam is aligned with the γ-Ga_2O_3–[1 1 1] direction for the spectra in Figure 2b. The obtained mismatch between the two is 2.9 ± 0.3° in χ (tilt angle). This observation is consistent with previous electron backscatter diffraction (EBSD) results presented in ref. [10], which report a slight misalignment between the otherwise fixed orientations of the β substrate and γ layer. The sample irradiated with 3.5×10^{14} ion cm^{-2} (light green) shows a slightly higher backscattering yield than the virgin (grey) sample due to the implantation-induced damage, but it still has good channeling properties and is far from the yield expected for an amorphous sample represented by the spectra obtained in a random orientation (black). There is a clear increase of the backscattering yield upon irradiation with 3.5×10^{15} ion cm^{-2}, shown in Figure 2a. At this fluence, the transformation is not finished (see Figure 1a) and the highly damaged mixed β/γ layer has a high dechanneling rate. As will be further discussed in the DB-VEPAS results, the high backscattering yield under this irradiation condition is attributed to the high concentration of defects. Note that the yield drops again beyond a depth of 200 nm which is deeper than the projected range of 140 keV Ne^+ (≈ 170 nm, calculated using SRIM[26]). The drop indicates the transition from the irradiated/disordered β/γ layer to the underlying ordered/unirradiated β substrate. Further increase of the fluence to 3.5×10^{16} ion cm^{-2} and beyond does not result in an increase of the channeling yield in case the ion beam is aligned parallel to the [$\bar{2}$ 0 1] direction of β-Ga_2O_3, as illustrated in Figure 2a. Note that [$\bar{2}$ 0 1] direction is not the ($\bar{2}$ 0 1) plane normal in β-Ga_2O_3 due to the non-orthogonal structure of the monoclinic lattice. However, the previously observed drop in the yield shifts to greater depth (≈ 285 nm at 3.5×10^{16} ion cm^{-2}) with increasing fluence and corresponds well with the measurements performed in TEM

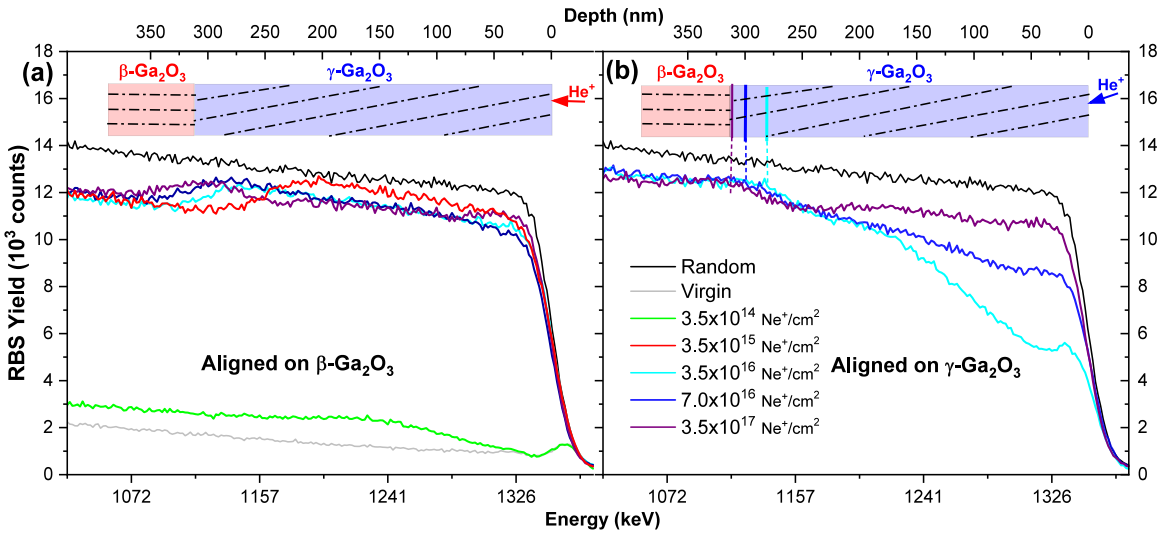

Figure 2. RBS/c spectra for β-Ga_2O_3 irradiated with different fluences. The irradiated area is converted from β-Ga_2O_3 to γ-Ga_2O_3 for 3.5×10^{16} ion cm^{-2} and higher fluences. a) RBS/c spectra obtained after aligning to the [$\bar{2}$ 0 1] β-Ga_2O_3 channeling direction. b) RBS/c spectra obtained after the phase transformation and realignment to the [1 1 1] γ-Ga_2O_3 channeling direction. The dashed lines in the sample configuration inset are only a sketch of the lattice planes and do not represent the actual misalignment. Of note, the depth scale is calculated for gallium atoms.

(260 nm). Additionally, if we realign the beam to the channeling direction in γ-Ga_2O_3, as illustrated in Figure 2b, the yield decreases significantly in the converted layer. The RBS/c yield increases toward the lower energy part of the spectra and stays close to the random case after 285 nm. The latter fact is not surprising, as the beam is now misaligned with respect to the β-Ga_2O_3–[$\bar{2}$ 0 1] direction in the β-Ga_2O_3 bulk. Furthermore, the characteristic shape and reasonable crystallinity are maintained for an irradiation fluence of 7×10^{16} ion cm^{-2}, corresponding to 52 dpa. A significant increase of the RBS/c yield in the first 150 nm is expected, since the maximum of the energy loss profile is at ≈ 115 nm for 140 keV Ne^+ ion implantation (see Note S2, Supporting Information, for SRIM calculation results), where the majority of the dpa is generated. Finally, after implantation of 3.5×10^{17} ion cm^{-2}, corresponding to 260 dpa, the measurements result in a very high RBS/c yield, close to but not fully reaching the amorphous case. Since the beam is aligned with the γ layer, we assume that it has a high number of defects and APBs in the existing γ phase, which consequently increases the RBS/c yield. This is also evident from the XRD results presented in Figure 1b.

We performed DB-VEPAS and VEPALS measurements (see **Figure 3**) to study the changes in defect type, structure, and concentration, for the β-to-γ phase transition. The detailed descriptions of these techniques are provided in the method section and elsewhere.[29] These methods utilize the effect that neutral and negatively charged vacancies, vacancy clusters, dislocations, or other open volume defects can trap positrons, where the relative contributions of valence and core electrons to the annihilation process varies, thus providing information about the local chemical environment (DB-VEPAS). In addition, the lifetime of positrons in the material is affected by the local electron density (VEPALS). While DB-VEPAS provides combined information on both the identity and concentration of positron traps, the lifetime results obtained from VEPALS offers complementary information by additionally quantifying the size of the defects.

In Figure 3a,c, the S-parameter is plotted as a function of the positron implantation energy and mean positron implantation depth for the reference sample and various irradiation fluences used in this study (see Supplementary Note 3 for S-W fractions). After irradiation with 3.5×10^{14} ion cm^{-2}, a "plateau" in the S-parameter values is observed, indicating an increase of the defect density. The S-parameter scales with the number of free volumes as long as positrons cannot easily diffuse due to a sufficient number of traps. With a further increase to 3.5×10^{15} ion cm^{-2}, a similar trend is observed, however with even greater S-parameter values in the plateau. When the defect concentration increases, there are more sites where positrons can get trapped and annihilate with low-momentum electrons, leading to an elevated S-parameter. The observation gets supported by the calculation of the defect concentrations using VEPfit code,[30] and the results are summarized in **Table 1** (see Experimental Section for details on the calculation). Note that the results obtained from the trapping of the positron is dominated by negatively charged defects and positively charged vacancies do not contribute to the effective defect concentration as measured by DB-VEPAS. These positively charged vacancies—specifically, oxygen vacancies in our case—exhibit low positron trapping rates and small positron binding energies due to Coulomb repulsion. Moreover, their open volumes are too small to support a trapped state in simulations, therefore, oxygen vacancies do not trap positrons according to existing calculations.[27] Thus, by using the term "defect concentration," we in fact present the perspective observed by positrons—an effective cation vacancy density.

As shown in Table 1, samples irradiated with 3.5×10^{14} ion cm^{-2} and 3.5×10^{15} ion cm^{-2} have shorter positron diffusion length and higher defect concentration than the reference sample. This is in line with the earlier described increased RBS/c yield (see Figure 2a) for these irradiation conditions (3.5×10^{14} ion cm^{-2} and 3.5×10^{15} ion cm^{-2}), which is an indication for an increased defect concentration. Interestingly, the previously

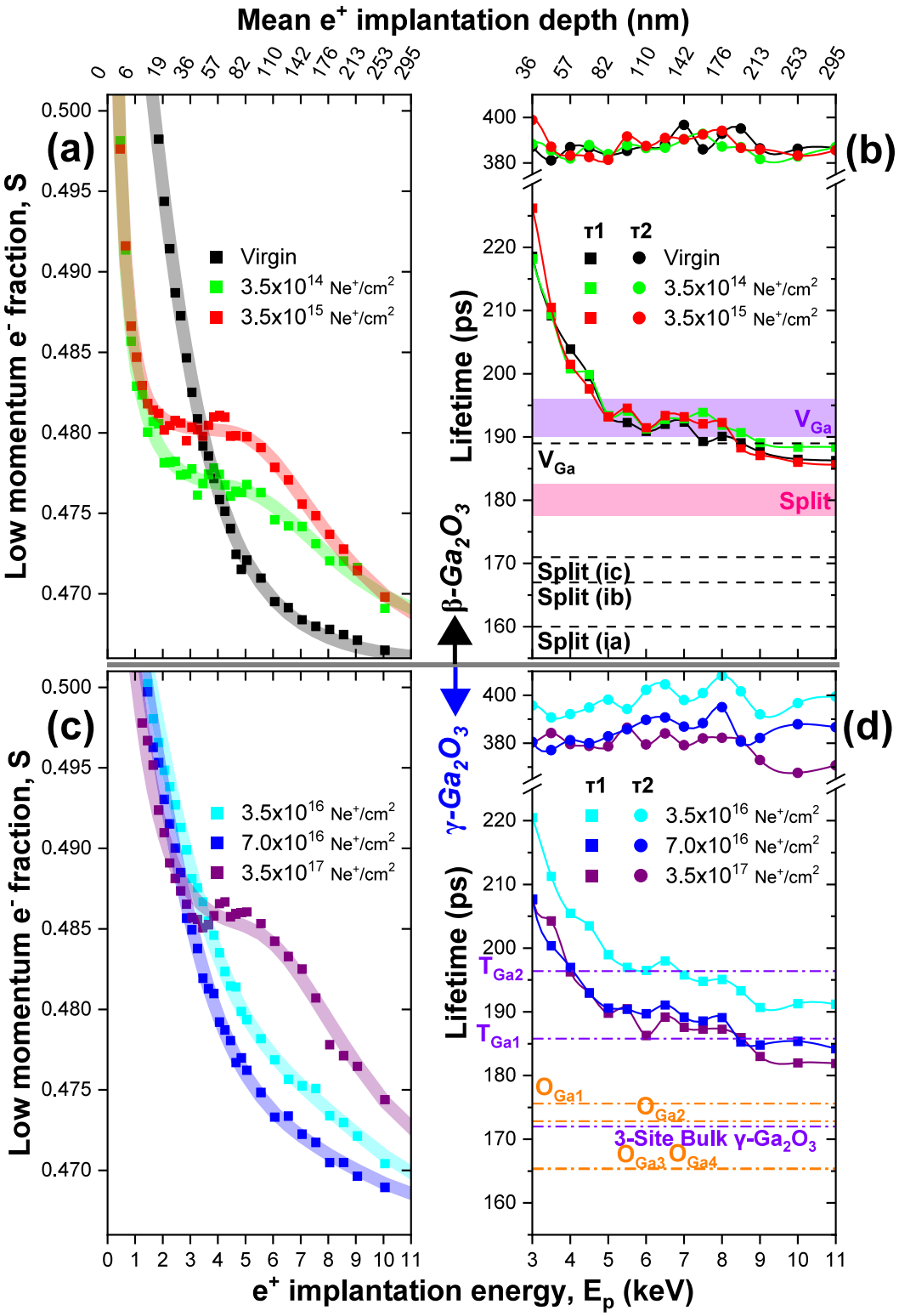

Figure 3. DB-VEPAS and VEPALS results for Ne $^{+}$ -irradiated samples with different fluences. Panels (a) and (c) show the S-parameter as a function of the positron implantation energy, and panels (b) and (d) show the positron lifetime as a function of the positron implantation energy. The colored transparent lines in (a) and (c) represent the fitted S-parameter curves generated from variable energy positron fitting (VEPfit) for each sample. The dashed lines in (b) represent theoretically calculated lifetimes for various defect configurations in β-Ga_2O_3,[27] while the violet and pink bar correspond to lifetimes of the different defect configurations as interpreted by Tuomisto for Fe-doped β-Ga_2O_3.[28] The dashed lines in (d) represent theoretically calculated lifetimes for various defect configurations in γ-Ga_2O_3 (see Table 2).

Table 1. VEPfit analysis results for 140 keV Ne $^+$ irradiations of β-Ga_2O_3. The defect concentration is calculated considering our β-Ga_2O_3 sample with the longest available effective diffusion length of 52.4 ± 0.5 nm.

Fluence	S-Parameter	W-Parameter	Diffusion length	Defective layer depth	Defect Concentration
[Neon cm^{-2}]	(Layer)	(Layer)	L+ [nm]	d [nm]	C_v [cm^{-3}]
0	0.4653(2)	0.0490(1)	27.7 ± 0.2	0	1.81×10^{18}
3.5×10^{14}	0.4765(2)	0.0446(1)	8.3 ± 0.5	182 ± 5	2.7×10^{19}
3.5×10^{15}	0.4801(1)	0.0449(1)	3.0 ± 0.2	171 ± 3	2.1×10^{20}
3.5×10^{16}	0.4722(2)	0.0485(1)	39.4 ± 0.4	325 ± 14	4.24×10^{17}
7×10^{16}	0.4694(2)	0.0500(1)	32.8 ± 0.3	326 ± 30	8.56×10^{17}
3.5×10^{17}	0.4847(1)	0.0468(1)	9.6 ± 0.2	211 ± 4	1.59×10^{19}

observed plateau in the S-parameter disappears after further increase of the irradiation fluence to 3.5×10^{16} ion cm^{-2} (see Figure 3c). From this, we can again calculate the defect concentration, which is $4.24 \times 10^{17} cm^{-2}$—three orders of magnitude lower as compared to the sample irradiated with only 1/10 of the fluence. This value, as is evident from Table 1, is also lower than that of the reference sample. However, from the above-presented XRD, TEM, and RBS/c results we know that this material is not β-Ga_2O_3 anymore but γ-Ga_2O_3. The decrease in defect density also explains the reduction in backscattering yield in the RBS/c signal within the first 200 nm for the sample irradiated with 3.5×10^{16} ion cm^{-2}, compared to the sample irradiated with 3.5×10^{15} ion cm^{-2}, as shown in Figure 2a. Increasing the irradiation fluence by a factor of two to 7×10^{16} ion cm^{-2} increases also the defect concentration by a factor of two (see Table 1). This is also evidenced from the steeper slope of the S-parameter depth profile, as plotted in Figure 3c. A further increase to 3.5×10^{17} ion cm^{-2} (260 dpa) causes the plateau in the S-parameter data to reappear in the sub–200 nm range, as can be seen in Figure 3c. As mentioned above, we attribute this to the accumulation of defects and an increase in their concentration. The position of the plateau also matches reasonably well with the prediction from SRIM for the maximum damage depth (see Note S2, Supporting Information). The high defect concentration for this sample goes hand in hand with the vanishing intensity of the γ-Ga_2O_3 related peaks in the XRD data presented in Figure 1b and the high RBS/c yield in Figure 2b.

Positron lifetime results for Ne $^+$-irradiated samples are plotted in Figure 3b,d. Since the relative intensity of the positron signals are dominated by the short-lived positrons (τ_1) rather than the long-lived positrons (τ_2)(see Note S3, Supporting Information), we will mainly focus on τ_1 lifetimes indicating small-sized defects such as monovacancies or other simple atomic-scale defects.[31] Theoretically calculated lifetimes for specific defects in β-Ga_2O_3, such as a gallium monovacancy ($V_{\{Ga\}}$) and a gallium split vacancy (Ga-divacancy with an interstitial Ga atom between two vicinal vacancies) are plotted as dashed lines in Figure 3b and correspond to 189 ps and 160 ps to 171 ps, respectively.[27] It should be noted that the approximations used by Karjalainen et al.[27] could lead to an underestimation of the lifetimes by not more than 10% due to the utilized Boroński-Nieminen local-density approximation.[32] Additionally, experimental lifetime measurements obtained on Fe-doped β-Ga_2O_3 crystals are plotted in Figure 3b at 190–196 ps (violet bar) and 177–183 ps (pink bar).[33,34] Tuomisto assigned these lifetimes to the $V_{\{Ga\}}$ and gallium split vacancies, respectively.[28] Upon careful inspection of Figure 3b, we see that the lifetime of the reference sample at 5–8 keV positron implantation energy is slightly higher than the theoretically expected 189 ps $V_{\{Ga\}}$ lifetime. On the other hand, they do match nicely with the experimental values obtained for irradiated Fe-doped β-Ga_2O_3.[33] These positron annihilation studies in the literature suggest that split vacancies are the dominant defect configuration in bulk β-Ga_2O_3.[33] The presence of $V_{\{Ga\}}$ defects in our case is most likely an artifact of the surface preparation and the resulting strain and damage (see Note S3, Supporting Information), contributing only insignificantly to the lifetimes reported in ref. [33], which were measured with fast positrons instead of VEPALS. However, also in our low-energy near-surface analysis, we see that with increasing depth, the observed lifetimes get closer to the expected split vacancy lifetime values from reference.[33] Additionally, the ratio curves generated from the coincidence Doppler broadening (cDB) spectra confirm that the split-vacancy configuration is expected in the deeper regions of the reference sample, while $V_{\{Ga\}}$ defect configuration is observed in the near-surface region (see Note S3, Supporting Information), further validating our findings.

After irradiation with 3.5×10^{14} ion cm^{-2} and 3.5×10^{15} ion cm^{-2}, the samples show similar positron lifetimes, indicating similar defect types. We therefore assume that in β-Ga_2O_3, after irradiation with 3.5×10^{14} ion cm^{-2} and 3.5×10^{15} ion cm^{-2}, we find a large number of $V_{\{Ga\}}$ similar to those of the reference sample, but at a significantly higher concentration as deduced from the DB-VEPAS results above. The measured positron τ_1 lifetimes for these two samples are longer than the theoretically calculated 189 ps for $V_{\{Ga\}}$. It is plausible that the irradiated samples in the depth range of 142 nm to 200 nm show, for example, a higher concentration of gallium divacancies ($2 \cdot V_{\{Ga\}}$) as they are easier to stabilize within the crystal, or larger complexes of a gallium vacancy with oxygen vacancies ($V_{\{Ga\}} + n \cdot V_O$, where $n > 1$), which increases the positron lifetime. Considering that theoretical models may underestimate positron lifetimes, it is possible that the observed disagreement is due to such an underestimation, and $V_{\{Ga\}}$ are indeed present in the irradiated samples. The cDB ratio curves further confirm this, indicating that the sample irradiated with 3.5×10^{15} ion cm^{-2} exhibits a $V_{\{Ga\}}$ defect configuration near the surface region (see Supplementary Note 3).

We also performed DFT calculations using the Vienna ab-initio simulation package (VASP) in order to obtain optimized bulk and defect configurations of the γ–phase. In the first place, we estimated the bulk positron lifetimes of the γ–phase for 2,

Table 2. Density functional calculations for the effect of different vacant ions on the positron lifetime. Ions at the tetrahedral ($T_{\{Ga\}}$) or octahedral ($O_{\{Ga\}}$) positions in the three-site γ-Ga_2O_3 model have been considered.

Ion	Nearest Neighbors (Ion-Distance [Å])		Lifetime
	Oxygen	Gallium	[ps]
Bulk			172
$T_{\{Ga1\}}$	1.83, 1.83, 1.88, 1.89	3.31, 3.33, 3.37, 3.40	186
$T_{\{Ga2\}}$	1.85, 1.85, 1.86, 1.86	3.07, 3.09, 3.23, 3.27	196
$O_{\{Ga1\}}$	1.93, 1.94, 1.98, 1.98, 2.06, 2.07	2.84, 2.94, 2.95, 3.16	176
$O_{\{Ga2\}}$	1.91, 1.92, 1.99, 2.04, 2.06, 2.07	2.87, 2.89, 2.94, 3.02	173
$O_{\{Ga3\}}$	1.94, 1.95, 1.96, 1.96, 2.05, 2.05	2.88, 2.89, 2.89, 2.89	165
$O_{\{Ga4\}}$	1.93, 1.94, 1.98, 1.98, 2.06, 2.07	2.84, 2.89, 2.89, 2.94	196

3, and 4 site occupancy models (see Note S3, Supporting Information). These different site occupancy models are constructed using $1 \times 1 \times 3$ 160–atom cells and are idealized models from the literature.[35] The different γ–phase models exhibit different positron lifetimes because each model has a different localization of the positrons in the open volume (see Note S3, Supporting Information). In addition, for the 3-site γ-Ga_2O_3 model, which is the most energetically favorable structure for γ-Ga_2O_3,[35] we estimated the bulk positron lifetime to be 172 ps. Furthermore, we removed a gallium atom from either an octahedral ($O_{\{Ga1\}}$, $O_{\{Ga2\}}$, $O_{\{Ga3\}}$, $O_{\{Ga4\}}$) or tetrahedral ($T_{\{Ga1\}}$, $T_{\{Ga2\}}$) positions to simulate vacancy-induced positron trapping under non-equilibrium, irradiation-like conditions. The resulting positron lifetimes for these $V_{\{Ga\}>}$ configurations are listed in **Table 2**. As already stated above, it is important to note that the theoretical models used here may underestimate the positron lifetimes. However, we will focus on the values obtained from our theoretical calculations and interpret the experimental results accordingly.

Even though the theoretical positron lifetime of the 3-site bulk γ-Ga_2O_3 model (without added vacancies) is comparable to the split vacancy lifetimes of β-Ga_2O_3, e.g. that of the split-i_c configuration, the situation is different in the sense that the positron energy band is slightly dispersed as in the case of a free positron state (delocalized annihilation). We, therefore, interpret that the γ–phase can have a free positron state, but its lifetime can still be consistent with vacancies in the β–phase, since the positron mostly interacts with the vacant gallium sites in the γ–phase (see Note S3, Supporting Information).

In Figure 3d, we plotted the calculated positron lifetimes for the 3-site γ occupancy model with different gallium vacancy positions for the added vacancy. Assuming the same trapping coefficient in γ-Ga_2O_3 and β-Ga_2O_3, the increased lifetime for the irradiation with 3.5×10^{16} ion cm^{-2} (see Figure 3d) could be explained by the increased size of the positron traps in the γ–phase compare to the β–phase. The measured positron lifetime of the sample irradiated with 3.5×10^{16} ion cm^{-2} is in good agreement with the calculated lifetime for the 3-site γ occupancy model when we create a $V_{\{Ga\}}$ on the $T_{\{Ga2\}}$ position (see Table 2). This suggests that after the ion-induced phase transition, the previously observed defect accumulation vanishes (compare Figure 3a with Figure 3c), and the γ–phase achieves its lowest energy configuration with additional $V_{\{Ga\}}$ at the $T_{\{Ga2\}}$ positions. If a neon atom occupies isolated point defects (e.g., monovacancies), the positron lifetime would be strongly reduced, approaching values between those characteristic of $V_{\{Ga\}}$ and the bulk. However, we do not observe such lifetimes in our measurements.

Examining the positron lifetime results for the 7×10^{16} ion cm^{-2} implantation in Figure 3d, a significant reduction to ≈ 190 ps is observed, which is in between the DFT-obtained lifetimes for the $T_{\{Ga2\}}$ and $T_{\{Ga1\}}$ atomic configurations. Our interpretation of this fact is that the γ–phase reaches a saturation for gallium vacancies at $T_{\{Ga2\}}$ positions, and the creation of gallium vacancies at $T_{\{Ga1\}}$ positions occurs by further increasing the irradiation fluence from 3.5×10^{16} ion cm^{-2} to 7×10^{16} ion cm^{-2}. Therefore, the sample irradiated with 7×10^{16} ion cm^{-2} likely contains defects in the form of gallium vacancies at both $T_{\{Ga2\}}$ and $T_{\{Ga1\}}$ positions. An additional increase in fluence to 3.5×10^{17} ion cm^{-2} leads to a further decrease in the lifetime, now matching well with the calculated lifetime for $T_{\{Ga1\}}$, as shown in Figure 3d. Consequently, 3.5×10^{17} ion cm^{-2} irradiation conditions on β-Ga_2O_3, corresponding 260 dpa, create a γ-Ga_2O_3 with a high concentration (see Table 1) of gallium vacancies at the $T_{\{Ga1\}}$ position. The average threshold displacement energy (TDE) for gallium vacancies at tetrahedral sites (22.9 eV) is higher than for the gallium vacancies at octahedral sites (20 eV).[36] However, TDE is highly direction dependent in γ-Ga_2O_3, resulting in a higher TDE along the [1 1 1] lattice direction for gallium vacancies at octahedral sites than for tetrahedral sites.[36] Based on the results presented in Figure 3d, we can conclude that the formation of $V_{\{Ga\}}$ on octahedral sites is unlikely in our samples. The increased defect concentration (see Table 1), while showing similar relative intensities for τ_1 and τ_2 (see Note S3, Supporting Information), suggests that even if these defects are present, their detection is likely hindered by saturation trapping, with $V_{\{Ga\}}$ on tetrahedral sites being dominant. It is worth noting that the implantation fluence of 3.5×10^{17} ion cm^{-2} corresponds to a peak neon concentration of ≈20 at.% in the implanted region, therefore neon bubble formation is likely in this sample. This is inline with the above observations that the γ 444 peak disappears at this fluence (see Figure 1b) and the increased dechanneling in the RBS measurements (see Figure 2b). In this case, implanted neon atoms accumulate in the voids, leading to the formation of bubbles, similar to the well known helium bubble formation.[37,38] positron annihilation spectroscopy (PAS) can reliably resolve defect clusters up to about 15 vacancies; for larger clusters, where the expected lifetimes are in the 350–450 ps range, precise identification becomes more challenging.[39] The size of the neon bubbles formed at this fluence (1–5 nm) can be significantly larger and will not contribute the the observed positron lifetimes. Smaller neon filled clusters are likely responsible for the observed small reduction of the τ_2 lifetime for 3.5×10^{17} ion cm^{-2} (see Figure 3d).

Figure 4 summarizes the evolution of the positron lifetimes and their relative intensities as a function of fluence. As expected, little or no change is observed for τ_1 and τ_2 and their relative intensities before the phase transition from β-Ga_2O_3 to γ-Ga_2O_3. Once the phase transition from β-Ga_2O_3 to γ-Ga_2O_3 occurs between 3.5×10^{15} ion cm^{-2} and 3.5×10^{16} ion cm^{-2}, a distinct change is observed in all four monitored VEPALS values, as shown in Figure 4a,b. The change in lifetimes is expected, as

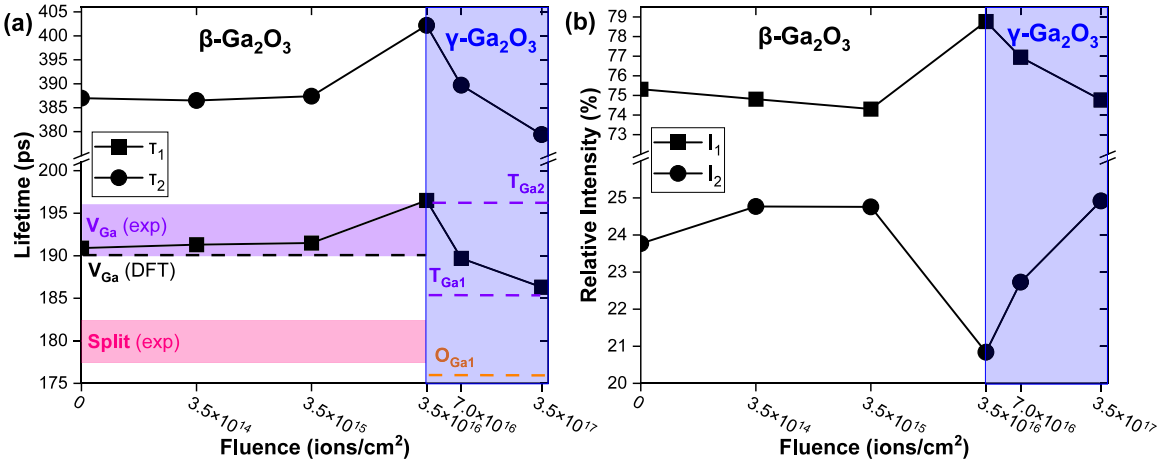

Figure 4. VEPALS lifetimes and relative intensities as a function of irradiation fluence obtained at a positron energy of 6 keV or in depth of 110 nm. a) Positron lifetimes of τ_1 (fast annihilation pathway) and τ_2 (slow annihilation pathway) as a function of irradiation fluence. b) Relative intensities of the short positron lifetime τ_1 (I_1) and long positron lifetime τ_2 (I_2) as a function of irradiation fluence.

the newly formed γ-Ga_2O_3 has a defective spinel structure with more open volume as compared to the monoclinic crystal structure of β-Ga_2O_3. As shown above, the new τ_1 lifetime corresponds to the calculated lifetimes of the $T_{\{Ga2\}}$ defects obtained from our DFT calculations. However, also the relative intensities of τ_1 and τ_2 change, as shown in Figure 4b, indicating a relative increase of small-volume defects and a relative decrease of large-volume defects after the phase transition. Increasing the irradiation fluence further leads to a decrease in both τ_1 and τ_2 lifetimes, with τ_1 eventually approaching the DFT-calculated $T_{\{Ga1\}}$ lifetime value. The observed changes in the relative intensities of the lifetime components suggest an increase in the proportion of vacancy clusters relative to single vacancies. This is expected, as higher irradiation fluences promote the aggregation of single vacancies into larger defect structures.

In conclusion, we performed a multi-method analysis approach to investigate the defect structure of the β-Ga_2O_3 to γ-Ga_2O_3 phase transition. XRD analysis of $(\bar{2}01)$-oriented β-Ga_2O_3 following 140 keV Ne^+ irradiation indicates a phase transition occuring above a certain fluence threshold. TEM imaging confirms the transition from the monoclinic to a defective spinel cubic crystal structure and reveals a transformed layer approximately 260 nm thick. Enhanced crystal quality was observed in the RBS/c spectra following the completion of the γ-Ga_2O_3 phase transition. DB-VEPAS and VEPALS were employed to utilize the sensitivity of positrons as atomic-scale probes for non-destructive measurement and characterization of defects, such as single vacancies and their agglomerates. VEPfit results show a reduced defect concentration and an increased positron diffusion length after irradiation with a fluence of 3.5×10^{16} ion cm^{-2}, which serve as a clear signature of the ion-induced phase transition. This reduced defect concentration is also in accordance with the enhanced crystal quality observed by RBS/c, after the phase transformation. Positron lifetimes calculated for the three-site γ-Ga_2O_3 phase model show an excellent agreement with the experimental results. Notably, the reduction in positron lifetime with increasing irradiation fluence in γ-Ga_2O_3 is an unexpected behavior for many other semiconductor materials and is a unique characteristic of γ-Ga_2O_3. We attribute this to the increased formation of different gallium vacancy positions in the 3-site γ-Ga_2O_3 model at high damage levels, which have a shorter positron lifetime. Our results show that the relatively good crystalline quality as observed by XRD and RBS/c in heavily irradiated Ga_2O_3 is related to a) the change in polymorph at around 3.5×10^{16} ion cm^{-2} (in the case of 140 keV Ne^+ irradiation) and b) the dominant formation of further defects in the already defective spinel structure of γ-Ga_2O_3 at specific tetrahedral sites in the cubic lattice. At high irradiation fluences, saturation of gallium vacancies at $T_{\{Ga2\}}$ sites and their aggregation into larger defect clusters are observed. Continued irradiation leads to the formation of single vacancies at $T_{\{Ga1\}}$ sites. This shift in vacancy formation within the γ phase may explain and contribute to the high radiation tolerance of the β/γ dual-phase polymorphic structure.

3. Experimental Section

Commercial $(\bar{2}\ 0\ 1)$-oriented β-Ga_2O_3 wafers from Novel Crystal Technology Inc. were irradiated with Ne^+ ions at an energy of 140 keV. The applied fluence ranged from 3.5×10^{14} ion cm^{-2} to 3.5×10^{17} ion cm^{-2} (see Table 1). The irradiations were performed at the Ion Beam Center of the Helmholtz-Zentrum Dresden-Rossendorf using a 500 keV implanter (High Voltage Engineering Europa B.V., Model B8385). Irradiations were performed using a 7° sample tilt to avoid channeling effects, and the maximum sample temperature during implantation was ≈ 60 °C. All samples, measuring 10 ×5 mm, were clamped at one corner and mounted on an aluminum plate for irradiation. Samples irradiated with fluences of 3.5×10^{14} ion cm^{-2} and 3.5×10^{15} ion cm^{-2} were exposed to an ion flux of 1.41×10^{12} ion cm^{-2} s^{-1}. For higher fluences, a water-cooled mounting plate was used, and the ion flux was increased to ≈5.82×10^{12} ion cm^{-2} s^{-1}.

X-ray diffraction (XRD) measurements were carried out as $\theta/2\theta$ scans on a Rigaku SmartLab 3kW diffractometer with a Cu X-ray tube operated at 40 kV and 50 mA. A Ge (2 2 0) channel-cut monochromator limited the spectrum of the parallel beam to the $K_{\alpha 1}$ line at 0.15406 nm. The sample was aligned in ω (incident angle) and χ (tilt angle) by its $\bar{2}01$ reflection of the β-Ga_2O_3 with the [1 0 2] direction parallel to the incident X-ray beam (at $\omega = 0$).

Cross-sectional TEM lamella preparation was carried out by in situ lift-out using a Thermo Fisher Helios 5 CX focused ion beam (FIB)-SEM device. To protect the sample surface, a carbon cap layer was deposited beginning with electron-beam-induced and subsequently followed by Ga-FIB-induced precursor decomposition. Afterward, the TEM lamella was prepared using a 30 keV Ga-FIB with adapted currents. Its transfer to a 3-post copper lift-out grid (Omniprobe) was done with an EasyLift EX nanomanipulator (Thermo Fisher). To minimize sidewall damage, Ga ions with 5 keV energy were used for final thinning of the TEM lamella to electron transparency. For comparison, a classical TEM cross-section, glued together in face-to-face geometry using G2 epoxy glue (Gatan), was prepared by sawing (Wire Saw WS 22, IBS GmbH), grinding (MetaServ 250, Bühler), polishing (Minimet 1000, Bühler), dimpling (Dimple Grinder 656, Gatan), and final Argon ion milling (Precision Ion Polishing System PIPS II 695, Gatan). BF-STEM imaging and convergent beam electron diffraction (CBED) (CBED beam diameter about 3 nm) were performed with a Talos F200X microscope (FEI) operated at an accelerating voltage of 200kV. HRTEM images were acquired with an image-C_s-corrected Titan 80-300 microscope (FEI) operated at 300 kV. FFT analysis was done based on the recorded HR-TEM micrographs. Prior to (S)TEM analysis, the specimen mounted in a double-tilt low-background holder was placed for 8 seconds into a Model 1020 Plasma Cleaner (Fischione) to remove potential contamination.

The used Rutherford backscattering spectrometry (RBS) setup was connected to a 2 MV Van de Graaff accelerator, and a 1.7 MeV $^4He^+$ beam was used for all measurements. The RBS/c measurements were performed along ($\bar{2}$ 0 1) β-Ga_2O_3 and (1 1 1) γ-Ga_2O_3 directions using a 170° backscattering geometry. Notably, Ga parts of the RBS/c data were used in the analysis because of the significantly higher sensitivity of this method for the heavier Ga sublattice compared to the O sublattice. Alignments for RBS/c to the β-Ga_2O_3 and γ-Ga_2O_3 were performed using a ±4° rectangular frame scan. For determining the channeling dips in β-Ga_2O_3 and γ-Ga_2O_3, the energy ranges of 0.99 Mev to 1.15 MeV and 1.24 MeV to 1.32 MeV were integrated, respectively. The minima obtained were used to find the planar channeling conditions, and the axial channeling conditions were subsequently calculated based on geometrical considerations.

DB-VEPAS measurements were conducted at the apparatus for in situ defect analysis (AIDA)[40] of the slow positron beamline (SPONSOR).[41] The kinetic energies of the positrons were adjusted to a discrete, monoenergetic values in the range of E_p= 0.05–35 keV enabling their implantation into defined depths. The mean positron implantation depth $< z >$ was approximated using a simple-material-density (ρ) dependent formula:[42]

$$< z > [nm] = \frac{36}{\rho[g \cdot cm^{-3}]} E_p^{1.62}[keV] \quad (1)$$

$< z >$ provides only a qualitative definition of the depth, while it does account for positron diffusion, however, is more accurate for materials with larger defect density. In general, during implantation, positrons lose their kinetic energy due to thermalization and, after short diffusion, annihilate in delocalized lattice sites or localize in point defects and their agglomerations, emitting at least two anti-collinear 511 keV gamma photons once they collide with electrons. The thermalized positrons have negligible momentum compared to the electrons, hence a broadening of the 511 keV line is the consequence of the electron momentum. All the signals were measured with one or two high-purity Ge detectors (energy resolution of 1.09 ± 0.01 keV or 0.78 ± 0.02 keV at 511 keV for single- and double-detector configuration, respectively). The broadening of the 511 keV line is typically characterized by the two distinct parameters S and W defined as a fraction of the annihilation distribution in the middle (511 ± 0.84 keV) and outer regions (503.4 keV–508.12 keV and 513.88 keV–518.61 keV), respectively. The total area below the curve, which is utilized for the normalization of both parameters, is 511.00 keV ± 16.24 keV.

The S-parameter is the fraction of positrons annihilating with low-momentum valence electrons and represents vacancy-type defects and their concentration. The W-parameter approximates overlap of positron wavefunction with high-momentum core electrons. Plotting the calculated S as a function of positron implantation energy, $S(E_p)$, provides depth-dependent information, whereas S-W plots are used to examine the atomic surrounding of the annihilation site and defect types.[43]

The cDB measurements of the annihilation peak, where both annihilation photons are simultaneously recorded have been employed to investigate the atomic surrounding of the defect site. Typically, every chemical element has an unique shape of the cDB spectrum. Since thermalized positrons have negligible momentum compared to electrons, the effective momentum of annihilating electron-positron pair consist mostly of the electron momentum. As the consequence, measured Doppler shift in the energy of the annihilation-photons yields the momentum distribution of electrons that have annihilated positrons. In addition such a coincidence measurement suppresses the accidental events from the background by recording only events of the simultaneous detection of both annihilation-photons. The difference in energies of the two annihilation photons is $E_1 - E_2 = 2 \cdot \Delta E = c \cdot p_L$, where c is the speed of light and p_L is the longitudinal component of the electron momentum to the direction of emitted annihilation photon.[44] cDB analysis has been conducted for the reference sample as well as for a characteristic ion fluence in order to discuss qualitative difference between the split and monovacancy defect configurations. The experimental findings have been compared with the theoretical considerations (see Supplementary Note 3).

Variable energy positron annihilation lifetime spectroscopy (VEPALS) measurements were conducted at the Mono-energetic Positron Source (MePS) beamline at HZDR, Germany.[29] A $CeBr_3$ scintillator detector coupled to the Hamamatsu R13089-100 photomultiplier tube (PMT) was utilized for gamma photons detection. The signals were processed by the SPDevices ADQ14DC-2X digitizer (14 bit vertical resolution and 2 GS/s horizontal resolution).[45] The overall time resolution of the measurement system was better than 0.250ns and all spectra contained at least 1×10^7 counts. A typical lifetime spectrum $N(t)$, the absolute value of the time derivative of the positron decay spectrum, is described by

$$N(t) = R(t) * \sum_{i=1}^{k+1} \frac{I_i}{\tau_i} e^{\frac{-t}{\tau_i}} + \text{“Background”} \quad (2)$$

where k is the number of different defect types contributing to the positron trapping, which are related to $k+1$ components in the spectra with the individual lifetimes τ_i and intensities I_i ($\sum I_i = 1$).[31] The instrument resolution function $R(t)$ is a sum of two Gaussian functions with distinct intensities and relative shifts, both depending on the positron implantation energy, E_p. It was determined by the measurement and analysis of a reference sample, i.e. single crystal yttria-stabilized zirconia, which exhibited a single well-known lifetime component. The background was negligible, hence fixed to zero. All the spectra were deconvoluted using a non-linear least-squares fitting method, minimized by the Levenberg-Marquardt algorithm, employed within the fitting software package PALSfit[46] into 2 major lifetime components, which directly evidence localized annihilation at 2 different defect types (sizes; τ_1 and τ_2). Their relative intensities scale typically with the concentration of each defect type. In general, positron lifetime increases with defects size and open volume size. The positron lifetime and its intensity were probed as a function of positron implantation energy E_p which was recalculated to the mean implantation depth $< z >$. The average positron lifetime τ_{av} is defined as $\tau_{av} = \sum \tau_i I_i$.

Defect concentrations mentioned in the text and Table 1 were calculated with the formula:

$$c_\nu = \frac{N}{\nu_\nu \tau_B} \left(\frac{L_{+,B}^2}{L_+^2} - 1 \right) \quad (3)$$

where N is the theoretical atomic density, $\nu_\nu = 1 \times 10^{15} s^{-1}$ is the positron trapping coefficient, τ_B is the measured positron lifetime, $L_{+,B}^2 = 52.4 \pm 0.5$ nm is the bulk positron diffusion length obtained from our best-quality reference sample, and L_+^2 is the effective positron diffusion length calculated from VEPfit. The atomic densities of β-Ga_2O_3 and γ-Ga_2O_3 were estimated as $N_\beta = 9.45 \times 10^{22} at\,cm^{-3}$ and $N_\gamma = 9.54 \times 10^{22} at\,cm^{-3}$, respectively.

$\tau_{B,\beta}$ = 135 ps and $\tau_{B,\gamma}$ = 173 ps for β-Ga_2O_3 and γ-Ga_2O_3 were adopted from[27] and our DFT calculations.

The positron states and annihilations in the β– and γ–phases of Ga_2O_3 were modeled using electronic structure methods and two-component theory for electron–positron systems.[32] The results for the β–phase are obtained by projecting the 3D momentum density data calculated in an earlier work,[27] and the γ–phase calculations were performed in this study. Here, the VASP code,[47,48] the projector augmented-wave (PAW) method,[49,50] and the generalized gradient approximation for electron-electron exchange and correlation effects.[51] were used. For the electron–positron correlation effects, the Boroński-Nieminen local-density approximation was used.[32] We assume that the localized positron does not influence the average electron density and take zero-positron-density limits of the correlation potential and enhancement factor. The momentum density of annihilating pairs is calculated using the state-dependent model,[52] reconstructed PAW wave functions for valence electrons,[53,54] and atomic orbitals for core electrons. Orientational averaging of the Doppler spectra was performed considering all possible orientations of the cubic γ supercells. Finally, before comparing with experiments, the Doppler spectra were convoluted with the experimental resolution function. The DFT calculations were based on the structural models reported by Ratcliff et al.,[35] which represent the most energetically stable configurations for each occupancy model in γ-Ga_2O_3. Given the intrinsic disorder of the Ga-sublattice, three distinct models were considered—2-site, 3-site, and 4-site—each corresponding to structures with two, three, and four occupied Ga sites, respectively.

Supporting Information

Supporting Information is available from the Wiley Online Library or from the author.

Acknowledgements

The authors acknowledge the M-ERA.NET Program for financial support via the GOFIB project supported by the tax funds on the basis of the budget passed by the Saxonian state parliament in Germany and administrated in Finland by the Research Council of Finland project number 352518. U.B., G.H., and N.K. acknowledge support by the COST Action CA19140 FIT4NANO. This research was carried out at the Ion Beam Center and ELBE at the Helmholtz-Zentrum Dresden-Rossendorf e. V., a member of the Helmholtz Association. The authors would like to thank the facility staff for assistance. The authors gratefully acknowledge Paul Chekhonin for his invaluable contributions to the CBED analysis, and extend sincere thanks to Romy Aniol and Andreas Worbs for their expert assistance with TEM specimen preparation. This work was partially supported by the Initiative and Networking Fund of the Helmholtz Association (FKZ VH-VI-442 Memriox) and the Helmholtz Energy Materials Characterization Platform (03ET7015). The authors are grateful for CSC -Finnish IT Center for Science for generous computational resources.

Conflict of Interest

The authors declare no conflict of interest.

Data Availability Statement

The data that support the findings of this study are openly available in RODARE at https://dx.doi.org/10.14278/rodare.3706, reference number 1.

Keywords

defects, gallium oxide, positron annihilation spectroscopy, power electronics

Received: April 17, 2025
Revised: September 12, 2025
Published online:

[1] R. Qiao, H. Zhang, S. Zhao, L. Yuan, R. Jia, B. Peng, Y. Zhang, *J. Phys. Appl. Phys.* **2022**, *55*, 383003.
[2] K. N. Heinselman, D. Haven, A. Zakutayev, S. B. Reese, *Cryst. Growth Des.* **2022**, *22*, 4854.
[3] S. J. Pearton, J. Yang, P. H. Cary, F. Ren, J. Kim, M. J. Tadjer, M. A. Mastro, *Applied Physics Reviews* **2018**, *5*, 1.
[4] P. Seyidov, J. B. Varley, Z. Galazka, T.-S. Chou, A. Popp, A. Fiedler, K. Irmscher, *APL Materials* **2022**, *10*, 11.
[5] A. Azarov, V. Venkatachalapathy, L. Vines, E. Monakhov, I.-H. Lee, A. Kuznetsov, *Applied Physics Letters* **2021**, *119*, 18.
[6] A. Sardar, T. Isaacs-Smith, J. Lawson, T. Asel, R. B. Comes, J. N. Merrett, S. Dhar, *Appl. Phys. Lett.* **2022**, *121*, 26.
[7] I. López, K. Lorenz, E. Nogales, B. Méndez, J. Piqueras, E. Alves, J. A. García, *Journal of Materials Science* **2013**, *49*, 1279.
[8] M. Sarwar, R. Ratajczak, C. Mieszczynski, A. Wierzbicka, S. Gieraltowska, R. Heller, S. Eisenwinder, W. Wozniak, E. Guziewicz, *Acta Materialia* **2024**, *268*, 119760.
[9] K. Lorenz, M. Peres, M. Felizardo, J. G. Correia, L. C. Alves, E. Alves, I. López, E. Nogales, B. Méndez, J. Piqueras, M. B. Barbosa, J. P. Araújo, J. N. Gonçalves, J. Rodrigues, L. Rino, T. Monteiro, E. G. Villora, K. Shimamura, In F. H. Teherani, D. C. Look, D. J. Rogers, editors, *Oxide-based Materials and Devices V*, volume *8987*. SPIE, ISSN 0277-786X, **2014** 89870M.
[10] A. Azarov, J. G. Fernández, J. Zhao, F. Djurabekova, H. He, R. He, Ø. Prytz, L. Vines, U. Bektas, P. Chekhonin, N. Klingner, G. Hlawacek, A. Kuznetsov, *Nat. Commun.* **2023**, *14*, 1.
[11] A. Azarov, C. Radu, A. Galeckas, I. F. Mercioniu, A. Cernescu, V. Venkatachalapathy, E. Monakhov, F. Djurabekova, C. Ghica, J. Zhao, A. Kuznetsov, *Nano Letters* **2025**.
[12] A. Y. Polyakov, A. A. Vasilev, A. I. Kochkova, I. V. Shchemerov, E. B. Yakimov, A. V. Miakonkikh, A. V. Chernykh, P. B. Lagov, Y. S. Pavlov, A. S. Doroshkevich, R. S. Isaev, A. A. Romanov, L. A. Alexanyan, N. Matros, A. Azarov, A. Kuznetsov, S. Pearton, *J. Mater. Chem. C* **2024**.
[13] K. Akaiwa, K. Kaneko, K. Ichino, S. Fujita, *Jpn. J. Appl. Phys.* **2016**, *55*, 121202BA.
[14] A. Y. Polyakov, E. B. Yakimov, V. I. Nikolaev, A. I. Pechnikov, A. V. Miakonkikh, A. Azarov, I.-H. Lee, A. A. Vasilev, A. I. Kochkova, I. V. Shchemerov, A. Kuznetsov, S. J. Pearton, *Crystals* **2023**, *13*, 1400.
[15] M. M. Islam, M. O. Liedke, D. Winarski, M. Butterling, A. Wagner, P. Hosemann, Y. Wang, B. Uberuaga, F. A. Selim, *Sci. Rep.* **2020**, *10*, 1.
[16] M. D. McCluskey, *J. Appl. Phys.* **2020**, *127*, 10.
[17] E. Korhonen, F. Tuomisto, D. Gogova, G. Wagner, M. Baldini, Z. Galazka, R. Schewski, M. Albrecht, *Appl. Phys. Lett.* **2015**, *106*, 24.
[18] J. Zhao, J. G. Fernández, A. Azarov, R. He, Ø. Prytz, K. Nordlund, M. Hua, F. Djurabekova, A. Kuznetsov, *Physical Review Letters* **2025**, *134*, 126101.
[19] A. Azarov, V. Venkatachalapathy, P. Karaseov, A. Titov, K. Karabeshkin, A. Struchkov, A. Kuznetsov, *Scientific Reports* **2022**, *12*, 1.
[20] H.-L. Huang, J. M. Johnson, C. Chae, A. Senckowski, M. H. Wong, J. Hwang, *Applied Physics Letters* **2023**, *122*, 25.
[21] R. He, J. Zhao, J. Byggmästar, H. He, F. Djurabekova, *Physical Review Materials* **2024**, *8*, 084601.
[22] J. García-Fernández, S. B. Kjeldby, P. D. Nguyen, O. B. Karlsen, L. Vines, Ø. Prytz, *Appl. Phys. Lett.* **2022**, *121*, 19.
[23] T. Yoo, X. Xia, F. Ren, A. Jacobs, M. J. Tadjer, S. Pearton, H. Kim, *Appl. Phys. Lett.* **2022**, *121*, 7.

[24] J. García-Fernández, S. B. Kjeldby, L. J. Zeng, A. Azarov, A. Pokle, P. D. Nguyen, E. Olsson, L. Vines, A. Kuznetsov, Prytz, *Materials Advances* **2024**, *5*, 3824.
[25] J. Tang, K. Jiang, C. Xu, M. J. Cabral, K. Xiao, L. M. Porter, R. F. Davis, *APL Materials* **2024**, *12*, 1.
[26] J. F. Ziegler, M. D. Ziegler, J. P. Biersack, *Nucl. Instrum. Methods Phys. Res. Sect. B Beam Interact. Mater. At.* **2010**, *268*, 11–121818.
[27] A. Karjalainen, V. Prozheeva, K. Simula, I. Makkonen, V. Callewaert, J. B. Varley, F. Tuomisto, *Phys. Rev. B* **2020**, *102*, 195207.
[28] F. Tuomisto, *Jpn. J. Appl. Phys.* **2023**, *62*, SFSF0802.
[29] A. Wagner, M. Butterling, M. O. Liedke, K. Potzger, R. Krause-Rehberg, *AIP Conf. Proc.* **2018**, *1970*, 040003.
[30] A. S. Saleh, *Journal of Theoretical and Applied Physics* **2013**, *7*, 39.
[31] R. Krause-Rehberg, H. S. Leipner, *Positron annihilation in semiconductors: defect studies*, June. Springer Berlin, Heidelberg, **1999**.
[32] E. Boroński, R. M. Nieminen, *Phys. Rev. B* **1986**, *34*, 3820.
[33] A. Karjalainen, I. Makkonen, J. Etula, K. Goto, H. Murakami, Y. Kumagai, F. Tuomisto, *Applied Physics Letters* **2021**, *118*, 7.
[34] A. Karjalainen, P. M. Weiser, I. Makkonen, V. M. Reinertsen, L. Vines, F. Tuomisto, *Journal of Applied Physics* **2021**, *129*, 16.
[35] L. E. Ratcliff, T. Oshima, F. Nippert, B. M. Janzen, E. Kluth, R. Goldhahn, M. Feneberg, P. Mazzolini, O. Bierwagen, C. Wouters, M. Nofal, M. Albrecht, J. E. N. Swallow, L. A. H. Jones, P. K. Thakur, T.-L. Lee, C. Kalha, C. Schlueter, T. D. Veal, J. B. Varley, M. R. Wagner, A. Regoutz, *Adv. Mater.* **2022**, *34*, 37.
[36] H. He, J. Zhao, J. Byggmästar, R. He, K. Nordlund, C. He, F. Djurabekova, *Acta Mater.* **2024**, *276*, 120087.
[37] F. I. Allen, *Beilstein Journal of Nanotechnology* **2021**, *12*, 633.
[38] G. Hlawacek, A. Gölzhäuser, *Helium Ion Microscopy*, Springer International Publishing, Switzerland **2016**, https://doi.org/10.1007/978-3-319-41990-9.
[39] J. Čížek, *Journal of Materials Science and Technology* **2018**, *34*, 577.
[40] M. O. Liedke, W. Anwand, R. Bali, S. Cornelius, M. Butterling, T. T. Trinh, A. Wagner, S. Salamon, D. Walecki, A. Smekhova, H. Wende, K. Potzger, *J. Appl. Phys.* **2015**, *117*, 163908.
[41] W. Anwand, G. Brauer, M. Butterling, H. R. Kissener, A. Wagner, *Defect Diffus. Forum* **2012**, *331*, 25.
[42] J. Dryzek, P. Horodek, *Nucl. Instrum. Methods Phys. Res. Sect. B* **2008**, *266*, 4000.
[43] M. Clement, J. M. M. de Nijs, P. Balk, H. Schut, A. van Veen, *J. Appl. Phys.* **1996**, *79*, 9029.
[44] J. Čížek, *J. Mater. Sci. Technol.* **2018**, *34*, 577.
[45] E. Hirschmann, M. Butterling, U. Hernandez Acosta, M. O. Liedke, A. G. Attallah, P. Petring, M. Görler, R. Krause-Rehberg, A. Wagner, *J. Instrum.* **2021**, *16*, 08P08001.
[46] J. V. Olsen, P. Kirkegaard, N. J. Pedersen, M. Eldrup, *Phys. Status Solidi C* **2007**, *4*, 4004.
[47] G. Kresse, J. Furthmüller, *Nato. Sc. S. Ss. Iii. C. S.* **1996**, *6*, 15.
[48] G. Kresse, J. Furthmüller, *Phys. Rev. B* **1996**, *54*, 11169.
[49] P. E. Blöchl, *Phys. Rev. B* **1994**, *50*, 17953.
[50] G. Kresse, D. Joubert, *Phys. Rev. B* **1999**, *59*, 1758.
[51] J. P. Perdew, K. Burke, M. Ernzerhof, *Phys. Rev. Lett.* **1996**, *77*, 3865.
[52] M. Alatalo, B. Barbiellini, M. Hakala, H. Kauppinen, T. Korhonen, M. J. Puska, K. Saarinen, P. Hautojärvi, R. M. Nieminen, *Phys. Rev. B* **1996**, *54*, 2397.
[53] I. Makkonen, M. Hakala, M. J. Puska, *J. Phys. Chem. Solids* **2005**, *66*, 1128.
[54] I. Makkonen, M. Hakala, M. J. Puska, *Phys. Rev. B* **2006**, *73*, 035103.